









Efficient energy transport throughout conical implosions

Yihang Zhang ¹ Zhe Zhang ^{1,2,3,*} Xiaohui Yuan,^{4,2} Kevin Glize ^{4,2} Xu Zhao,^{4,2} Ke Fang ¹ Chenglong Zhang,^{1,5} Yufeng Dong,^{1,6} Shaojun Wang ^{1,6} Xuejie Bai,⁷ Bingjun Li ⁷ Zhengdong Liu,^{8,9} Huigang Wei,¹⁰ Dawei Yuan ¹⁰ Fuyuan Wu,^{4,2} Yanfei Li,⁷ Jiayong Zhong,^{8,2,9} Yutong Li,^{1,2,6,3} and Jie Zhang ^{1,4,2,†}

¹Beijing National Laboratory for Condensed Matter Physics, Institute of Physics, Chinese Academy of Sciences, Beijing 100190, China

²Collaborative Innovation Center of IFSA (CICIFSA), Shanghai Jiao Tong University, Shanghai 200240, China

³Songshan Lake Materials Laboratory, Dongguan 523808, China

⁴MoE Key Laboratory for Laser Plasmas and School of Physics, Shanghai Jiao Tong University, Shanghai 200240, China

⁵State Key Laboratory for Tunnel Engineering, China University of Mining and Technology, Beijing 100083, China

⁶School of Physical Sciences, University of Chinese Academy of Sciences, Beijing 100049, China

⁷Department of Nuclear Science and Technology, Xi'an Jiaotong University, Xi'an 710049, China

⁸Department of Astronomy, Beijing Normal University, Beijing 100875, China

⁹Institute for Frontiers in Astronomy and Astrophysics, Beijing Normal University, Beijing 102206, China

¹⁰Key Laboratory of Optical Astronomy, National Astronomical Observatories, Chinese Academy of Sciences, Beijing 100012, China



(Received 29 May 2023; accepted 12 February 2024; published 11 March 2024)

The double-cone ignition (DCI) scheme has been proposed as one of the alternative approaches to inertial confinement fusion, based on direct-drive and fast-ignition, in order to reduce the requirement for the driver energy. To evaluate the conical implosion energetics from the laser beams to the plasma flows, a series of experiments have been systematically conducted. The results indicate that 89%–96% of the laser energy was absorbed by the target, with moderate stimulated Raman scatterings. Here 2%–6% of the laser energy was coupled into the plasma jets ejected from the cone tips, which was mainly restricted by the mass reductions during the implosions inside the cones. The supersonic dense jets with a Mach number of 4 were obtained, which is favorable for forming a high-density, nondegenerated plasma core after the head-on collisions. These findings show encouraging results in terms of energy transport of the conical implosions in the DCI scheme.

DOI: [10.1103/PhysRevE.109.035205](https://doi.org/10.1103/PhysRevE.109.035205)

I. INTRODUCTION

Inertial confinement fusion (ICF) research aims at abundant clean energy production from light-element nuclear fusion process during the confinement provided by the mass inertia of the highly compressed fuel [1]. Most ICF schemes pursue an ignition initiated from a hot spot, which is created by efficient conversion from implosion mechanical work into internal energy. This requires that the energy carried by the α particles from the D-T fusion process inside the hot spot should be at least higher than the energy losses, while the α particles can be captured by the fuel to maintain self-sustained burning [2]. The highest fusion yield of more than 3.88 MJ on the National Ignition Facility (NIF) [3] marks a significant advance in ICF research, as it resulted in a target gain of 1.9. However, researchers are still striving to assess the stability in the burning plasma regime and optimize the fusion gain. In the vicinity of ignition, effects of instabilities seeded by varied sources would be accumulated and raised. While the cold fuel is heated with mass ablation and burn propagation, the hot spot could be significantly cooled due to fuel-ablator mix [4]. Especially for burning plasma regime, the hot spot with higher temperature offers α particles longer stopping ranges [5]. Thus, the performance for power balance gets

more fragile causing the burn quenching near the ignition cliff. To achieve a stable ignition and increase energy gain in ICF, it is necessary to understand the merit for implosion energetics, which allows for an optimization of the igniting trajectory.

To tackle the challenges in the pursuit of high-energy gain, the double-cone ignition (DCI) scheme was proposed [6], based on direct-drive [7] and fast-ignition [8] concepts. In the scheme, two gold cones are employed to confine part-shell implosions. The conically compressed fuel ejected from the head-on cone tip forms a high-velocity jet. The head-on collision of two jets from double cones makes them fuse to an isochoric-distributed fuel, with high density and sharp edge. As the jets stagnate during the collision, the kinetic energy transits to the internal one and the plasma becomes preheated. Finally, in the isochoric high-density plasma, a fast-electron beam guided by an external magnetic field [9–12] can deposit energy rapidly and adequately, and an ignited hot-spot forms. The schematic diagram of the four main steps of the DCI scheme is shown in Fig. 1(a), with the implosions, fast electrons, and magnetic field driven by about 10 ns, 10 ps, and 1 ns laser pulses, respectively. The general route of energy coupling and transition can be described as follows. As the laser beams propagate up the density gradient to the critical surface, they transfer energy to thermal electrons via the inverse bremsstrahlung absorption as the dominant mechanism [13]. In the meantime, part of the laser energy is diverted from the coronal plasma through laser-plasma instabilities

*zzhang@iphy.ac.cn

†jzhang1@sjtu.edu.cn

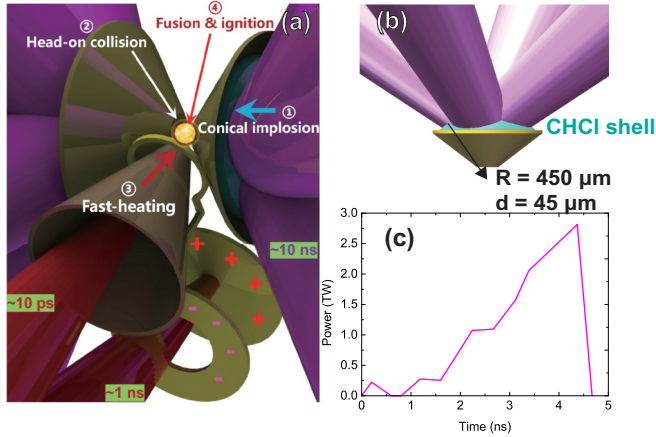


FIG. 1. (a) Schematic diagram for illustration of the DCI scheme. (b) Geometry of the conical irradiation on the shell-in-cone target. The CHCI shell is initially embedded in the gold cone, and four laser beams overlap at the shell surface through 525- μm continuous phase plates. (c) Laser temporal profile with overlapped power on the target noted in (b).

(LPIs) [14]. Moreover, the thermal-electrons transfer their energy to the plasma up to the ablation front through thermal conduction [15], then the corresponding shock wave [16] from the ablation front transports inward and heats the fuel shell. The ablated matter exhausts outward which leads to the shell inward implosion due to the momentum balance [17]. During the shell converging in the conical implosion, part of the kinetic energy is converted into internal energy, and the fuel gets precompressed. As the converged flows eject from two head-on tips and form high-speed jets, they collide with each other, and the sharp deceleration leads to efficient conversion from the kinetic energy into the internal one [18]. After the collision, a fast-electron beam driven by a high-power picosecond laser pulse heats the core to ignition condition. At last, the fuel releases an amount of fusion energy during the burning period. By carrying out laser irradiance with equivalent intensity at a part of a sphere, the DCI scheme relaxes the driver energy requirements for compression. The double-cone configuration also reserves entire space in the plane perpendicular to the cone axis, for additional heating cones allowing fast-electron injection.

In order to investigate the feasibility of the double-cone ignition scheme proposed in Ref. [6], the energy coupling and transport in the conical implosions have been studied experimentally and analytically, based on the DCI Round 6 experiment campaign. We report characteristics of three major parts of energy transport-laser energy absorption, the exhaust and implosion energy in the acceleration phase, and energy transition and losses in the coasting phase during conical implosion. The total laser absorption in a shell target inside a gold cone can be as high as 89%–96% with moderate LPI levels. At the end of the laser pulse, 73% of the laser energy has been allocated to the exhaust, and 12% coupled to the imploding shell. After the coasting phase, the imploding shell forms a supersonic dense jet with a Mach number of 4 ejected from the cone tip. The jet has carried 2%–6% of the laser energy, mainly restricted by mass reduction inside the

cone. The results could provide insights into the energetics figures of merit in the conical implosions and show basics on the restrictions. The implications are important on the further stages of head-on collision and fast heating in the DCI scheme.

II. RESULTS

A. Experimental setup

The experiments reported herein were carried out at the Shenguang-II upgrade laser facility [19]. The target consisted of a $\text{C}_{16}\text{H}_{14}\text{Cl}_2$ (CHCI) partial spherical shell embedded in a gold cone (shell-in-cone target) with a full opening angle of 100° . The inner diameter R and shell thickness d were 450 μm and 45 μm , respectively. The shell was irradiated by four laser beams on top at an angle of 50° to the polar axis, forming an axisymmetric conical irradiation, as shown in Fig. 1(b). Each beam delivered 1250 J energy onto the shell, as ultraviolet with 351-nm wavelength and focusing into a 525- μm diameter determined by a continuous phase plate. The temporally shaped low-entropy-compressing laser pulse [20] is shown in Fig. 1(c). The resulting intensity of four overlapped beams at maximum is $1.2 \times 10^{15} \text{ W/cm}^2$.

Understanding the energy coupling and transition processes requires characterizing the physical states during the implosions. The fraction of laser energy absorbed in the coronal plasma has been inferred from a quasiglobal angular-resolved diagnostics for the scattered light [21]. The energy contained in the exhaust plasma has been inferred through a 2D-framing x-ray penumbral imaging system [22] compared with the hydrodynamic simulations by the MULTI 1D code [23]. For the shell implosion inside the cone, as most of the emissions are blocked by the Au cone, the theory of ablative heat waves has been used to calculate the shell kinetic energy. The temperature of the shell coasting in the cone and ejected from the cone tip has been diagnosed by the streaked optical pyrometer (SOP) [24] facing through the tip to the shell inner surface, assuming it emits as a black-body radiator. The velocity and mass of the plasma jet at the cone-tip have been measured by an x-ray pinhole streak camera (XPSC) and a Cu-K_α backlight imager [25], respectively. The plasma temperature after head-on collisions has been monitored by a hard x-ray spectrometer to measure the Cl feature spectrum [26]. In effect, polystyrene deuteride C_8D_8 (CD) shells have been used as standard fuel for neutron generation from D-D reactions in the preliminary experiments of the DCI scheme. The CHCI material has been used to provide an efficient characterization of the plasma temperature and velocity due to brighter and detectable bremsstrahlung radiation induced from the moderate-Z Cl element. The near-constant mass absorption coefficient of CHCI plasma with wide ranges of temperature and density also provides accurate density characterization using Cu-K_α backlight. So in this paper, the energetics in each process are from the CHCI shell-in-cone targets to maintain consistency and remain systematic.

B. Laser absorption

The energy coupled from the incident laser beams to the plasma is restricted by the scattered light in LPI processes,

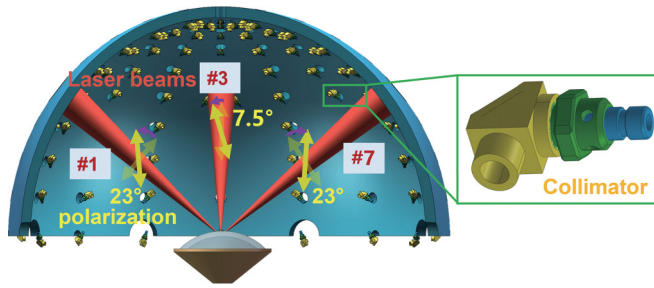


FIG. 2. Schematic diagram of the 60FSPM. 60 reflective collimators are set on the inner side of the chamber wall, collecting the light emitted from the laser-target interactions. The arrows represent the polarization directions (bright arrows) with respect to the p -polarization direction (shaded ones).

which would decrease the inward acceleration and generate hot electrons to increase the fuel entropy. In order to obtain overall characterization of LPs covering nontypical angles from the conical irradiation with the four beams on the shell-in-cone target, besides the full-aperture back-scattering station (FABS) of the Beam no. 7 [27], light emitted into the upper hemisphere has been measured by a 60-channel fiber spectrometer (60FSPM). The schematic diagram of the diagnostic is shown in Fig. 2. There were 60 reflective collimators collecting the light emitted from the laser-target interactions and reflecting it to 60 channels of the optical fiber bundle. The end of the bundle was coupled in a linear array into an optical spectrometer. With a 150 G/mm ruled grating, 60-channel optical spectra in 300–800 nm could be recorded by a charge-coupled-device (CCD) camera with a spectral resolution of 1.5 nm. Since the polarization of the four beams was symmetric about the polar axis (see Fig. 2), the measurement covering a quarter sphere could reveal the scattered lights in 2π solid

angle according to an axisymmetric assumption of the coronal plasma flow. The spectral response of the detector has been absolutely calibrated in energy for each fiber channel. The energy losses could be derived by spectral integration of the detected intensity. The 60FSPM could not only provide the laser absorption according to the total scattered energy, but also reveal LPI mechanisms through the light spectral characteristics.

For the shell-in-cone target, the overall energy measured by the 60FSPM and FABS occupy on average 6.9% and 1.4% of the laser energy, respectively, which reveals that 92% absorption has been obtained typically. The light on the 60FSPM is dominated by stimulated Raman scattering (SRS, 500–650 nm) [28,29], which accounts for 5.5% of the laser energy, as shown in the spectra in Fig. 3(a), while in the FABS most of the signal comes from the laser reflection around 351 nm, and scattering from the cross-beam energy transfer (CBET) [30,31] and stimulated Brillouin scattering (SBS) [32], which accounts for 1.3% of the laser energy on average. Here we do not wish to address an immediate realization of quantitative analysis for each LPI process, but to demonstrate the energy losses in emitted light from the plasma. Emissions near 702 nm, associated with the rescattering on the two-plasmon-decay (TPD) [33,34] plasma waves, have also been measured to be less than 0.7% and negligible. The summarized data are shown in Table I. The averaged values have been taken from 17 shots with similar laser and target conditions. Figure 3(b) shows the angular distribution of scattered light from the shell-in-cone target. Here the 0 degree of the polar angle is in the upper pole along the target normal, and Beam no, 3 is the origin of the azimuthal angle. Considering our moderate single-beam intensity and density scale length, the interaction is below the back SRS threshold, which has been discussed in detail in our separate work [27], and only the side SRS is responsible for the emissions. This is

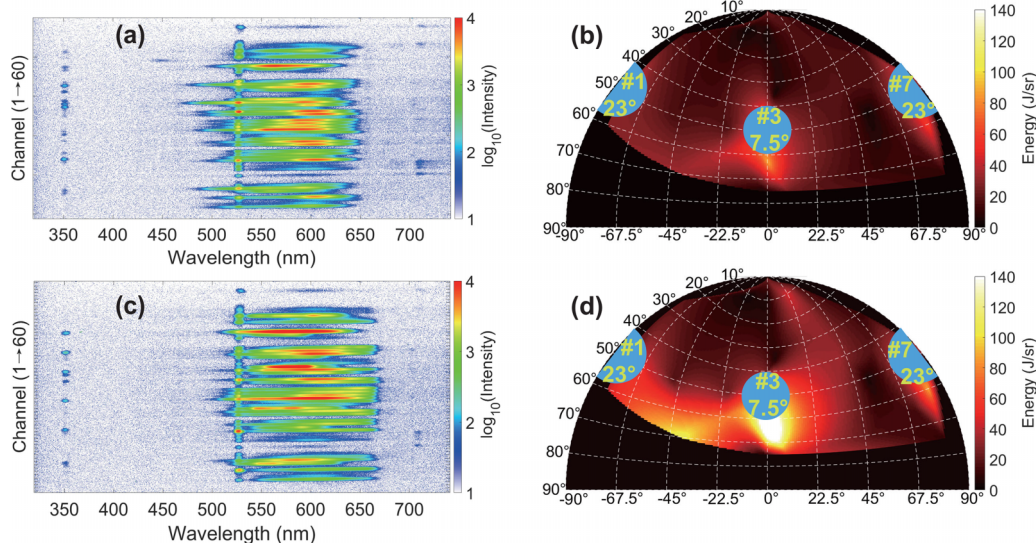


FIG. 3. Typical raw images of the scattered light spectra from the CHCl shell-in-cone (a) and planer (c) targets measured by the 60FSPM, with the longitudinal axis representing collectors at different orientations. The wavelength in spectra indicates different processes of LPs (spectral response needs to be taken into account for absolute energy calculation). The corresponding angular distributions of side-scattered lights are shown in (b) and (d), using linear interpolation for the directions between two adjacent collectors. In (b) and (d) the blue-shaded areas represent the directions of laser incidence, with the beam serial numbers and polarization angles.

TABLE I. Summary of energy scattered efficiency (normalized to the laser energy) due to 351-nm lights and SRS, and in total under the CHCl shell-in-cone and planar targets. Here Avg. represents the statistically averaged value from 17 shots with the same designed parameters of lasers and targets, and Max. and Min. are the maximum and minimum values, respectively.

	Shell-in-cone target					Planar target				
	351 nm		SRS		Total	351 nm		SRS		Total
	FABS	60FSPM	FABS	60FSPM		FABS	60FSPM	FABS	60FSPM	
Avg.	1.3%	1.4%	0.06%	5.5%	8.3%	2.8%	2.0%	0.09%	9.3%	14.2%
Max.	2.3%	1.8%	0.18%	6.3%	10.6%	3.6%	2.6%	0.12%	12.3%	18.6%
Min.	0.6%	1.0%	0.01%	2.5%	4.1%	1.9%	1.6%	0.05%	8.3%	11.9%

confirmed by that most of the light is scattered at polar angles larger than the laser incidence. Besides, due to the proximity of the emissions with the laser incidence, the scattering is more likely driven by single-beam-induced SRS.

In order to have a clear look at the characteristics of LPIs in the geometry with the shell-in-cone target, four-beam irradiations on 50- μm -thick CHCl planar targets with the same diagnostics have been taken as comparison experiments. In the case of the planar target, the total absorption is 85.8% on average, with 2.8% and 2.0% laser energy coupled to the 351-nm scattering in FABS and 60FSPM, respectively, and 0.09% and 9.3% laser energy to the SRS in the two diagnostics (see Table I). The spectra also show a dominantly broad feature of side SRS [see Figs. 3(c) and 3(d)]. Both Table I and Fig. 3 show weaker SRS in the shell-in-cone target compared with the planar one, on average by a factor of 1.7. One of the possible mechanisms is related to the coronal plasma geometry. According to the Rosenbluth gain formula [35,36], the amplification of SRS lights increases with the plasma scale length L_n . There is a shorter L_n due to the spherical expansion in the shell-in-cone target compared with a planar expansion. Essentially the propagation path is shorter for SRS energy gain [28], and it leads to reduction of scattered energy losses with the shell-in-cone target. To exclude the effects of Au contamination from the cone on LPIs and light absorption, experiments with pure CHCl shell (the same with the shell-in-cone target but without Au cone) targets have been carried out. The results from the 60FSPM show the scattered energy of 351 nm and SRS are $1.6 \pm 0.4\%$ and $4.0 \pm 0.3\%$ of the laser energy, respectively. Since the scattered energy is at a similar level as the CHCl shell-in-cone target, we consider the Au contamination has little effect on the laser absorption in the corona region.

C. Exhaust energy of the outward ablated material

During the laser and thermal-electron ablation, the exhaust energy of the ablated material (including corona and thermal conduction areas) takes much of absorbed energy, which limits the energy coupled to the inward implosion. On the other hand, however, the exhaust plasma accelerates the shell inward via the rocket effect, which ensures the kinetic energy of implosion. In principle, there is an optimized energy allocation for outward exhaust and inward implosion.

The temperature of exhaust material can be inferred from a 2D framing x-ray penumbral imaging measuring the self-emission in 0.1–10 keV on top of the irradiated surface. The

ablated plasma is consisting of the under-dense corona and dense thermal conduction area, which make the self-emitted soft x-ray with moderate photon energy in 0.1–10 keV a suitable probe. The x-ray framing camera uses 16 penumbral holes creating a 4×4 array of irradiated shell images, and the reconstructed images are shown in Fig. 4(a). Considering the penumbral imaging with a decoded technique and the framing camera system, a spatial resolution of $\Delta x = 10.4 \mu\text{m}$ has been achieved. In Fig. 4(a) the timings of the left images in the four strips are labeled, which are controlled by a delay box sending individual delay pulses with ± 200 ps jitter monitored by an oscilloscope. There are four images in each framing strip. The time separation between adjacent frames on the same strip is about 50 ps according to the sweeping speed of

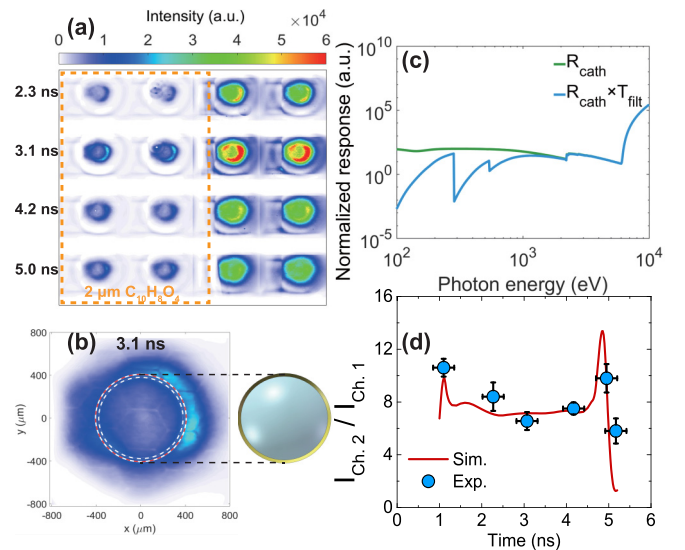


FIG. 4. (a) Reconstructed 16-framed images from the top view of the ablated plasma. The four strips in horizontal direction record at four different timings during the laser irradiation. (b) The first image on the second strip, where the dashed red and blue circles are corresponding to the initial outer edges of the cone and shell, respectively. A 2- μm -thick $\text{C}_{10}\text{H}_8\text{O}_4$ filter has been employed to measure the plasma parameters by the x-ray spectral absorption. The normalized spectral response of the system with and without filter is plotted in (c) as the blue and green curves, respectively. The averaged intensity ratio of the shell in the unfiltered and filtered channels is expressed as a function of time with fluctuations in different shots, as shown as the blue dots in (d), where the red curve is the intensity ratio calculated from the MULTI 1D simulation.

the high-voltage pulse on the Au photocathode. Figure 4(b) is the enlarged image at 3.1 ns, and the dashed red and blue circles are corresponding to the initial outer edges of the cone and shell, respectively. Under a nanosecond-long-pulse irradiation, assuming the ablated plasma evolution is gentle and negligible within 50 ps, images in adjacent frames are temporally close enough to apply an x-ray absorption filter method [37] for derivation of the ablated plasma temperature, by using 2- μm -thick $\text{C}_{10}\text{H}_8\text{O}_4$ (Mylar) filter for the early two frames in each strip. The x-ray energy spectral response for the filtered channel (called Ch. 1) is shown as the blue curve in Fig. 4(c), while the one for the bare channel (Ch. 2) is shown as the green curve, both of which have considered the effect of the Au photocathode.

For the coronal area, the plasma usually keeps nearly isothermal either by heat conduction or by direct laser deposition [38]. The under-dense plasma with temperature of several keV is optically thin compared with the Planck mean-free path, so the absorption is little for the soft x-ray self-emissions. However, in the dense matter ablated by thermal electrons with sharp density and temperature profiles, higher density brings stronger bremsstrahlung radiation while lower temperature leads to more absorption. Here we employed one-dimensional hydrodynamic simulation MULTI 1D to provide spatial profile and temporal evolution of plasma parameters. The parameters of density and temperature could set a reference to calculate the x-ray self-emission intensity and be compared with the experimental results, to provide possible solutions for the exhaust internal energy. As a low Z and nearly fully ionized material, the emitted x-rays can be assumed as bremsstrahlung radiations. Considering the response efficiency $R(\nu)$ for the photon energy ν induced by the Au cathode and filter, the intensity on the detector I_{Ch} can be expressed as follows, considering a transmission caused by the mass absorption coefficient μ (as a function of ν , local electron temperature T_e , and density ρ) and areal density (integration of ρ along the path x):

$$I_{\text{Ch}} = \int_0^L \int_0^\infty I_{\text{br}}(\rho, T_e, \nu) R(\nu) \times \exp\left[-\int_x^L \mu(\rho, T_e, \nu) \rho dx'\right] d\nu dx, \quad (1)$$

where $I_{\text{br}}(\rho, T_e, \nu) \propto \rho^2 T_e^{-1/2} \exp(-h\nu/T_e)$ is determined by the bremsstrahlung spectral energy emission per volume, and L is the path length. The intensity ratio in the shell region between channels without and with the filter $I_{\text{Ch},2}/I_{\text{Ch},1}$ is plotted against time in Fig. 4(d), where the red curve is calculated from the MULTI 1D simulation, and the blue dots are from experimental measurements. The error bars in the horizontal axis are owing to the time jitter of the framing camera, while the ones in the vertical axis are from the systematic errors of the measured intensity ratios from a series of shots. Taking the error bars into account, the simulation well predicts the experimental results, except for the data around 2.3 ns, which might come from differences between the experimental pulse shapes and the original design (see Fig. 5). According to this comparison, at the measured timings, density-weighted electron temperature in the ablated plasma could be derived from the simulation, shown as the green dots in Fig. 5,

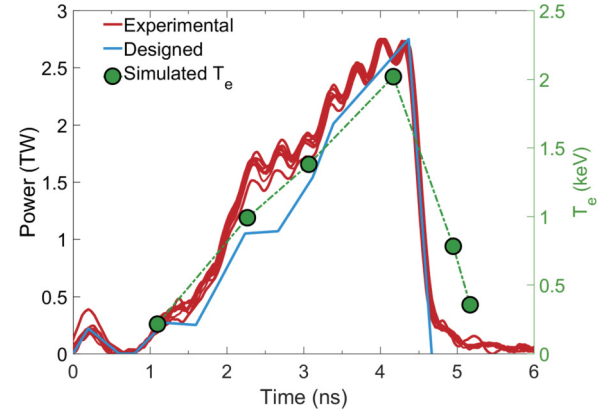


FIG. 5. Temperature evolution of the exhaust plasma (green circles), which represents the density averaged electron temperature derived from the MULTI 1D simulation. The pulse shapes from multiple experimental shots and the design are shown as the red and blue curves, respectively.

representing temporal evolution of the heating effect in the exhaust material. The electrons in the ablated plasma are heated from 0.2 keV at 1.1 ns, to 2.0 keV at 4.2 ns.

The theory on Coulomb collisions elucidates that equilibrium between electrons and ions is hard to be obtained in plasma with high temperature and low density in a nanosecond timescale. It is necessary to plug both electron T_e and ion temperature T_i with the density ρ from the simulation into estimation of the exhaust internal energy. As plasma exhausting with low density, the weakly interacting particles can be described as a classical ideal gas and the internal energy is proportional to the temperature. The exhaust internal energy at the end of the laser pulse could be calculated as

$$E_{\text{int}} = \frac{3}{2\bar{m}_i} \int_0^L \rho(r) k_B [ZT_e(r) + T_i(r)] S(r) dr = 1169 \text{ J}, \quad (2)$$

where $S(r)$ is the shell area at the radial position r , assuming a spherical expansion. \bar{m}_i is the average ion mass in a CHCl molecule, and k_B is the Boltzmann constant. Here T_e , T_i , and ρ are from the MULTI 1D simulation.

As the plasma exhausts from the ablation front to the under-dense corona, it is pushed by the pressure gradient from the area with higher density to lower density region, and accelerated to higher velocity. From the simulation the exhaust kinetic energy at the end of the laser pulse can be obtained by the following integration, according to the exhausting velocity $v_{\text{ex}}(r)$:

$$E_{\text{kin}} = \frac{1}{2} \int_0^L \rho(r) v_{\text{ex}}^2(r) S(r) dr = 2482 \text{ J}, \quad (3)$$

In the limiting case of a plane isothermal flow with an exponential density gradient, v_{ex} increases linearly with the distance from the ablation front [39], and the kinetic energy content equals 1.7 times of the internal one. However, the realistic situation should consider the spherical expansion as well as the nonlocal laser absorption before the critical surface via inverse bremsstrahlung. The kinetic energy has a higher

percentage as 2.1 times of the internal one in our case, compared with stationary cases.

D. Inward energy transport in the conical implosion

The inward implosion of the shell is driven by the ablated material expanding outward due to momentum conservation. According to the theory of ablative heat waves driven by inverse bremsstrahlung absorption, the mass ablation rate and ablation pressure of fully ionized CHCl can be expressed as $\dot{m} = 3.5 \times 10^4 I_L^{5/9} \lambda_L^{-4/9} r_f^{-2/9}$ and $P_{\text{abl}} = 1.4 I_L^{7/9} \lambda_L^{-2/9} r_f^{-1/9}$, where I_L and λ_L are the laser intensity and wavelength, respectively, while r_f is the focal radius [40]. Considering the laser pulse shape and conical geometry [41], the fractional payload of a CHCl shell is 54%, which means an imploding shell mass $M_{\text{res}} = 13.2 \mu\text{g}$. From the momentum of the expelled mass, the ablated plasma has velocity $v_{\text{ex}} = P_{\text{abl}}/\dot{m} = 4.0 \times 10^{-5} I_L^{2/9} \lambda_L^{2/9} r_f^{1/9}$. The ablated mass can be written as $M_{\text{abl}}(t) = \int_0^t \dot{m} S(t') dt'$. Here $S(t')$ is the shell area varying with time during the forward implosion. From the ablated mass M_{abl} and expansion velocity v_{ex} , the implosion velocity can be evaluated through the momentum conservation as $v_r = \int_0^t \dot{m} S(t') \frac{v_{\text{ex}}}{M_0 - M_{\text{abl}}(t')} dt' = 302 \text{ km/s}$. This provides a maximum value for imploding kinetic energy of 594 J, 12% of the laser energy, at the end of the laser pulse. At the same time, the SOP indicates the inner shell is heated to the temperature of $15 \pm 3 \text{ eV}$. At this temperature with over-dense density, the fuel is in the warm dense plasma regime and nonideal plasma effects occur. The degeneracy (ratio of the thermal energy to Fermi one) Θ is a function of the electron temperature T_e and density n_e , as $\Theta = (\hbar^2/2m_e)^{-1} k_B T_e (3\pi^2 n_e)^{-2/3}$. The density at the end of the laser is not measured, as the diagnostic field of view is blocked by the cone. But it can be assumed that $\rho \leq 5.1 \text{ g/cm}^3$ as an upper limit of the density at the center of double cones at 5.8 ns (1.3 ns after the laser pulse), when the head-on plasma jets have just started to collide with each other [42]. A collisional-radiative spectral analysis code PrismSPECT [43] has been used to solve the ionization state of the CHCl plasma according to the temperature and mass density, and then the free electron density n_e could be derived. Thus, the degeneracy is in the range of $\Theta \geq 0.6$, which indicates the fuel could be considered as a partially degenerate Fermi gas. The internal energy can be determined by two parts including partially degenerate electrons and classical ions, $E_{\text{int}} = E_e + E_i = 3/2(pV + N_i k_B T_i)$, where N_i and T_i are the number and temperature of ions. The relation $E_e = 3/2 pV$ is valid for a Fermi gas at any degeneracy [1]. The volume V could be expressed by M_{res}/ρ . The electron pressure p can be written as $p = p_F(5/2\Theta + \frac{X\Theta^{-\gamma} + Y\Theta^{(\gamma-1)/2}}{1+X\Theta^{-\gamma}})$, with the Fermi pressure $p_F = 2/5 n_e (\hbar^2/2m_e)(3\pi^2 n_e)^{2/3}$ and constants $X = 0.27232$, $Y = 0.145$, and $\gamma = 1.044$. Assuming in the dense plasma the electrons and ions could be balanced quickly in a sub-nanosecond timescale [1], i.e., $T_e = T_i = T_{th}$ is valid, the internal energy of the imploding fuel at the end of the compressing laser pulse is in a range of $6.6 \text{ J} < E_{\text{int}} < 11.0 \text{ J}$, 0.12%–0.22% of the laser energy, with the lower and upper limits corresponding to classical plasma as an ideal gas and partly degenerate plasma with density of 5.1 g/cm^3 , respectively.

Considering an ideal conical implosion, the shell substantially coasts along the conical wall with a uniform radial velocity v_r and gets compressed as a converging hydrodynamic flow. The shell gets heated as the transverse (perpendicular to the cone axis) velocity vanishes during the convergence, and the corresponding kinetic energy is converted to the internal one. Assuming the longitudinal (parallel to the cone axis) motion hardly experience deceleration inside the cone, the velocity of the jet ejected from the cone tip v_y is an angular-averaged longitudinal component of v_r , among the spherical cap with an angle of 100° ,

$$v_y = \frac{\int_{-50^\circ}^{50^\circ} v_r \cos\theta d\theta}{\int_{-50^\circ}^{50^\circ} d\theta} = 265 \text{ km/s}. \quad (4)$$

The XPSC has recorded a 1D-spatial vs temporal trace [44], demonstrating that the longitudinal velocity of the jet from the cone tip reaches $240 \pm 25 \text{ km/s}$ in 5.3–5.7 ns, which has a similar level to v_y . The mass of the jet is $5.7 \pm 1.9 \mu\text{g}$, which is calculated as a half of the mass after the head-on collision from double cones, according to a 2D areal density map measured by a Cu-K α backlight imager at 6.0 ns, after the density reaches the peak value. Based on the mass and velocity measured by the two types of diagnostics, the corresponding kinetic energy in the jet is 87.8–266.9 J, 1.8%–5.3% of the laser energy. At 5.8 ns, when the plasma ejected from the cone tip, the brightness on the SOP shows the jet temperature reaches the maximum of $60 \pm 12 \text{ eV}$ as a result of the preheating through convergence. Assuming the density of the jet is 5.1 g/cm^3 (upper limit), the degeneracy Θ is 1.7 (above 1), so the jet at the cone tip could be approximately considered as a classical plasma. Thus, according to the temperature and mass, the internal energy $E_{\text{int}} = E_e + E_i = 3/2(N_e + N_i)k_B T = 11.4\text{--}34.1 \text{ J}$, 0.23%–0.68% of the laser energy.

Table II summarizes the energetics coupling efficiency from the laser, and the plasma parameters related to the energy values. Figure 6 shows a schematic diagram of the energy coupling route from the laser to the plasma jet at the cone tip. Here the letters I and K on the graph denote the internal and kinetic energy, respectively. In the conical implosion, 2%–6% of the 5000 J laser energy has been coupled into the plasma jet ejected from the cone tip, where the kinetic energy is 1.8%–5.3%.

III. DISCUSSION

According to the results demonstrated above, the averaged value of absorbed energy from laser is 4589 J, while the averaged total energy of the exhaust and implosion add up to 4254 J. It means there are about 335 J remaining from the absorbed energy. The energy loss via bremsstrahlung emission would not take as much as this order of magnitude in the low-Z CHCl plasma. In the realistic experiment, some minor lobes of the laser spot have irradiated the side wall of the Au cone and been absorbed in Au plasma, which is clearly seen from the x-ray emission image in Fig. 4(a). Assuming a 2- μm ablated depth in Au, and the same x-ray absorption of Au plasma with cold Au, rough electron temperature of 0.8 keV

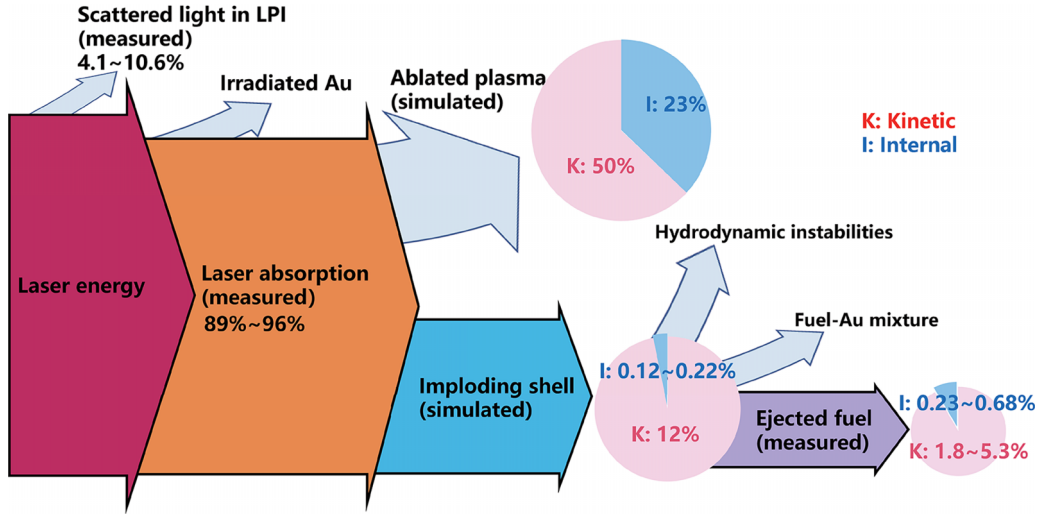


FIG. 6. Diagram of energy transport in the conical implosions, where the I and K are internal and kinetic energy, respectively, and the energetics are expressed as the coupling efficiency from the incident laser beams.

could be derived using the filter method, corresponding to internal energy of 300 J. Although the accurate energy absorbed by Au cone is unknown, it can be estimated semi-quantitatively through this method.

Aside from the LPIs and exhaust plasma, energy losses of the imploding plasma inside the cone is the main restriction for the energy coupling to the jet. The kinetic and internal energies of the jet predicted directly from the MULTI 1D simulation are 392 J and 93 J, corresponding to 7.8% and 1.9% of the laser energy, which is higher than the measured results. The simulation ignores multidimensional effects such as hydrodynamic instabilities and implosion asymmetry, which would lead to overestimation of the energy coupling. The analysis on the implosion energy shows the longitudi-

nal velocity keeps at a relatively steady level as the shell coasting inwards to the cone tip. The critical limiting factor on kinetic energy at the cone tip is the mass reduction from the 13.2 μg payload inferred from the ablation theory inside the cone to the $5.7 \pm 1.9 \mu\text{g}$ plasma jet at the cone tip. If the Rayleigh-Taylor instability (RTI) coupled to the shell grows in the acceleration and coasting stages, the tangential velocity increases around the RT spikes, a large amount of material could be taken away from the centripetal motion to the cone tip. Besides, the implosion asymmetry is a possible reason which leads to velocity distribution in the longitudinal space. As the $5.7 \pm 1.9 \mu\text{g}$ is a spatially integrated mass outside the cone tip at 0.1 ns after the peak colliding density, it is only a small portion from the imploding shell, while the follow-up ejection continues, but the fuel with lower velocity may have limited contribution to the high-density plasma formation in the head-on collision process.

In our experiment, the velocity of the plasma jet at the cone-tip is $240 \pm 25 \text{ km/s}$. According to the temperature at the tip measured by the SOP ($T_{th} = 60 \text{ eV}$), the sound velocity is $c_s = 61.8 \text{ km/s}$. The jet Mach number could be derived as

$$\mathcal{M} = v_y/c_s \approx 4. \quad (5)$$

When neglecting the effect of viscosity in the dynamic processes, the motion equation of the supersonic jet turns out to be

$$\frac{dv_y}{dt} = -\frac{1}{\rho} \frac{dp}{dy} = -\frac{1}{\rho} \frac{dp}{v_y dt}, \quad (6)$$

where $dp = (Z + 1)k_B/\bar{m}_i(\rho dT_{th} + T_{th}d\rho)$. From this and Eq. (5) it follows that

$$\frac{d\rho}{\rho} + \frac{dT_{th}}{T_{th}} \propto -\mathcal{M}^2 \frac{dv_y}{v_y}. \quad (7)$$

Equation (7) indicates that, in a head-on collision of jets with higher Mach numbers, especially for the supersonic jets, the relative variation of velocity could bring larger relative increase of density and temperature. This means the plasma jets are expectable to generate a high-density plasma core. In

TABLE II. Summary of energy coupling efficiency (normalized to the laser energy) and plasma parameters (mass, velocity, and temperature) in different processes of the conical implosion. The parameters of ablated plasma and imploding shell mass and velocity were calculated with simulations and theoretical formulas, and the energy of laser absorption and parameters of the fuel ejected from the cone as well as the temperature of the imploding shell were experimentally measured.

Laser absorption (measured)	Efficiency ^a	$92^{+4}_{-3}\%$
Ablated plasma (simulated)	Mass	11.2 μg
	Electron temperature	$\sim 2 \text{ keV}$
	Efficiency	73%
Imploding shell	Mass (simulated)	13.2 μg
	Imploding velocity (simulated)	302 km/s
	Plasma temperature (measured)	$15 \pm 3 \text{ eV}$
	Efficiency	12%
Ejected fuel (measured)	Mass	$5.7 \pm 1.9 \mu\text{g}$
	Ejecting velocity	$240 \pm 25 \text{ km/s}$
	Plasma temperature	$60 \pm 12 \text{ eV}$
	Efficiency	2%–6%

^aThe energy coupling efficiency from the incident laser beams.

addition, the quantum electron degeneracy effects still act in the warm-dense jets. The temperature enhancement during the head-on collisions would ensure the plasma to become non-degenerate, for efficient energy absorption during Coulomb collisions in the further fast-heating stage.

In previous DCI campaigns, supersonic collisions of such plasma jets with high Mach numbers have been verified to perform efficient transition from the kinetic to internal energy [18]. The 2%–6% energy coupling efficiency from the laser to the jet may substantially determine the energy coupled to the core after collision. This efficiency is at a similar level with the record energy coupling to a hot spot, inferred from typical literature for central ignition (about 2.9% inferred from direct drive [45], and 2.6%–3.2% from indirect drive including α particle heating [46]) and fast-ignition (about 2.2% before fast-heating [47]) schemes.

IV. CONCLUSIONS

An experimental investigation of energetics in the DCI scheme was conducted, with a comprehensive set of measurements tracking the energy transport in the whole conical implosion process. From the conversion efficiency between metrics for the energetics in each step, the energy loss mechanisms and its quantity can be indicated.

Under the conical irradiation with a peak laser intensity of 1.2×10^{15} W/cm², the total absorption by the shell-in-cone target has been measured as $92_{-3}^{+4}\%$ (in the format $average_{lower\ limit}^{upper\ limit}$), where the side SRS is up to $5.5_{-3.0}^{+0.8}\%$ of the laser energy dominating the energy losses through LPIs. The detailed comparison with a planar target reveals that the shell-in-cone geometry constrains the SRS growth, probably

due to the shorter density scale length in the coronal plasma. The x-ray framing imaging of the shell indicates that the absorbed energy has been partly taken away by the exhaust plasma (73% of the laser energy inferred by the MULTI 1D simulation) as well as the irradiated wall of the Au cone. The residual energy in the imploding shell is 12% of the laser energy, inferred from the ablation theory. During the shell coasting in the cone, there is 42%–71% of the mass reduction (from the 13.2 μ g payload to the 5.7 ± 1.9 μ g jet at the cone tip), but the longitudinal velocity of the jet keeps stable at a level similar with the imploding shell. Finally, 2%–6% of the laser energy is coupled into the high-density plasma jet at the cone tip. The major challenges of the scheme as inferred from the presented study is the fuel mass reduction during the implosion inside the cone. The Mach number of the jet is about 4. This is expected to generate high-density plasma core in the head-on collision process. Further improvement in implosion performance is possible if larger masses can be coupled to jets, by accurately estimating the hydrodynamic instability and active design on its inhibitions in the implosions. This work could advance the understanding of the physical mechanisms involved in the DCI scheme.

ACKNOWLEDGMENTS

This study was supported by the Strategic Priority Research Program of the Chinese Academy of Sciences (Grants No. XDA25010100, No. XDA25010300, No. XDA25030100, and No. XDA25030200) and also in part by the National Natural Science Foundation of China (Grants No. 11827807 and No.12105359).

-
- [1] S. Atzeni and J. Meyer-ter-Vehn, *The Physics of Inertial Fusion: Beam-Plasma Interaction, Hydrodynamics, Hot Dense Matter*, Vol. 125 (Oxford University Press, Oxford, 2004).
- [2] J. D. Lawson, Some criteria for a power producing thermonuclear reactor, *Proc. Phys. Soc. B* **70**, 6 (1957).
- [3] See <https://optics.org/news/14/11/38/> for the news of the NIF record.
- [4] B. Bachmann, S. A. MacLaren, S. Bhandarkar, T. Briggs, D. Casey, L. Divol, T. Döppner, D. Fittinghoff, M. Freeman, S. Haan *et al.*, Measurement of dark ice-ablator mix in inertial confinement fusion, *Phys. Rev. Lett.* **129**, 275001 (2022).
- [5] G. S. Fraley, E. J. Linnebur, R. J. Mason, and R. L. Morse, Thermonuclear burn characteristics of compressed deuterium-tritium microspheres, *Phys. Fluids* **17**, 474 (1974).
- [6] J. Zhang, W. M. Wang, X. H. Yang, D. Wu, Y. Y. Ma, J. L. Jiao, Z. Zhang, F. Y. Wu, X. H. Yuan, Y. T. Li, and J. Q. Zhu, Double-cone ignition scheme for inertial confinement fusion, *Phil. Trans. R. Soc. A* **378**, 20200015 (2020).
- [7] R. S. Craxton, K. S. Anderson, T. R. Boehly, V. N. Goncharov, D. R. Harding, J. P. Knauer, R. L. McCrory, P. W. McKenty, D. D. Meyerhofer, J. F. Myatt *et al.*, Direct-drive inertial confinement fusion: A review, *Phys. Plasmas* **22**, 110501 (2015).
- [8] M. Tabak, J. Hammer, M. E. Glinsky, W. L. Kruer, S. C. Wilks, J. Woodworth, E. M. Campbell, M. D. Perry, and R. J. Mason, Ignition and high gain with ultrapowerful lasers, *Phys. Plasmas* **1**, 1626 (1994).
- [9] T. Johzaki, K. Mima, S. Fujioka, H. Sakagami, A. Sunahara, H. Nagatomo, and H. Shiraga, Electron beam guiding by strong longitudinal magnetic fields, *J. Phys.: Conf. Ser.* **688**, 012041 (2016).
- [10] S. Kar, H. Ahmed, R. Prasad, M. Cerchez, S. Brauckmann, B. Aurand, G. Cantono, P. Hadjisolomou, C. L. S. Lewis, A. Macchi *et al.*, Guided post-acceleration of laser-driven ions by a miniature modular structure, *Nat. Commun.* **7**, 10792 (2016).
- [11] M. Bailly-Grandvaux, J. J. Santos, C. Bellei, P. Forestier-Colleoni, S. Fujioka, L. Giuffrida, J. J. Honrubia, D. Batani, R. Bouillaud, M. Chevrot *et al.*, Guiding of relativistic electron beams in dense matter by laser-driven magnetostatic fields, *Nat. Commun.* **9**, 102 (2018).
- [12] S. Sakata, S. Lee, H. Morita, T. Johzaki, H. Sawada, Y. Iwasa, K. Matsuo, K. F. F. Law, A. Yao, M. Hata *et al.*, Magnetized fast isochoric laser heating for efficient creation of ultra-high-energy-density states, *Nat. Commun.* **9**, 3937 (2018).
- [13] J. Dawson, P. Kaw, and B. Green, Optical absorption and expansion of laser-produced plasmas, *Phys. Fluids* **12**, 875 (1969).
- [14] D. H. Froula, D. T. Michel, I. V. Igumenshchev, S. X. Hu, B. Yaakobi, J. F. Myatt, D. H. Edgell, R. Follett, V. Y. Glebov, V. N. Goncharov *et al.*, Laser-plasma interactions in

- direct-drive ignition plasmas, *Plasma Phys. Control. Fusion* **54**, 124016 (2012).
- [15] S. X. Hu, V. A. Smalyuk, V. N. Goncharov, S. Skupsky, T. C. Sangster, D. D. Meyerhofer, and D. Shvarts, Validation of thermal-transport modeling with direct-drive, planar-foil acceleration experiments on OMEGA, *Phys. Rev. Lett.* **101**, 055002 (2008).
- [16] Ya. B. Zeldovich and Yu. P. Raizer, *Physics of Shock Waves and High Temperature Hydrodynamic Phenomena* (Academic Press, New York, 1967).
- [17] D. T. Michel, V. N. Goncharov, I. V. Igumenshchev, R. Epstein, and D. H. Froula, Demonstration of the improved rocket efficiency in direct-drive implosions using different ablator materials, *Phys. Rev. Lett.* **111**, 245005 (2013).
- [18] Z. Zhang, X.-H. Yuan, Y.-H. Zhang, H. Liu, K. Fang, C.-L. Zhang, Z.-D. Liu, X. Zhao, Q.-L. Dong, G.-Y. Liu *et al.*, Efficient energy transition from kinetic to internal energy in supersonic collision of high-density plasma jets from conical implosions, *Acta Phys. Sin.* **71**, 155201 (2022).
- [19] C. N. Danson, C. Haefner, J. Bromage, T. Butcher, J.-C. F. Chanteloup, E. A. Chowdhury, A. Galvanauskas, L. A. Gizzi, J. Hein, D. I. Hillier *et al.*, Petawatt and exawatt class lasers worldwide, *High Power Laser Sci. Eng.* **7**, e54 (2019).
- [20] F. Wu, X. Yang, Y. Ma, Q. Zhang, Z. Zhang, X. Yuan, H. Liu, Z. Liu, J. Zhong, J. Zheng, Y. Li, and J. Zhang, Machine-learning guided optimization of laser pulses for direct-drive implosions, *High Power Laser Sci. Eng.* **10**, e12 (2022).
- [21] Y. Zhang, Z. Zhang, X. Zhao, K. Glize, Y. Dong, X. Yuan, Y. Li, and J. Zhang, A global and full-spectral scattered light diagnostic for laser-plasma interaction studies (unpublished).
- [22] B. Bachmann, J. E. Ralph, A. B. Zylstra, S. A. MacLaren, T. Döppner, D. O. Gericke, G. W. Collins, O. A. Hurricane, T. Ma, J. R. Rygg *et al.*, Localized mix-induced radiative cooling in a capsule implosion at the national ignition facility, *Phys. Rev. E* **101**, 033205 (2020).
- [23] R. Ramis and J. Meyer-ter-Vehn, MULTI-IFE—A one-dimensional computer code for inertial fusion energy (IFE) target simulations, *Comput. Phys. Commun.* **203**, 226 (2016).
- [24] J. E. Miller, T. R. Boehly, A. Melchior, D. D. Meyerhofer, P. M. Celliers, J. H. Eggert, D. G. Hicks, C. M. Sorce, J. A. Oertel, and P. M. Emmel, Streaked optical pyrometer system for laser-driven shock-wave experiments on OMEGA, *Rev. Sci. Instrum.* **78**, 034903 (2007).
- [25] J. A. Koch, Y. Aglitskiy, C. Brown, T. Cowan, R. Freeman, S. Hatchett, G. Holland, M. Key, A. MacKinnon, J. Seely *et al.*, 4.5- and 8-keV emission and absorption x-ray imaging using spherically bent quartz 203 and 211 crystals (invited), *Rev. Sci. Instrum.* **74**, 2130 (2003).
- [26] Y. Dai, Y. Zhang, X. Yuan, Z. Zhang, Y. Dong, H. Gu, C. Zhang, Y. Li, and J. Zhang, Fast heating of double-cone ignition scheme measured by x-ray spectroscopy (unpublished).
- [27] K. Glize, X. Zhao, Y. H. Zhang, C. W. Lian, S. Tan, F. Y. Wu, C. Z. Xiao, R. Yan, Z. Zhang, X. H. Yuan, and J. Zhang, Measurement of stimulated Raman side-scattering predominance in directly driven experiment, *Phys. Plasmas* **30**, 122706 (2023).
- [28] P. Michel, M. J. Rosenberg, W. Seka, A. A. Solodov, R. W. Short, T. Chapman, C. Goyon, N. Lemos, M. Hohenberger, J. D. Moody *et al.*, Theory and measurements of convective Raman side scatter in inertial confinement fusion experiments, *Phys. Rev. E* **99**, 033203 (2019).
- [29] R. W. Short, Absolute stimulated Raman side scatter in direct-drive laser-produced plasmas, *Phys. Plasmas* **27**, 042703 (2020).
- [30] I. V. Igumenshchev, W. Seka, D. H. Edgell, D. T. Michel, D. H. Froula, V. N. Goncharov, R. S. Craxton, L. Divol, R. Epstein, R. Follett *et al.*, Crossed-beam energy transfer in direct-drive implosions, *Phys. Plasmas* **19**, 056314 (2012).
- [31] J. A. Marozas, M. Hohenberger, M. J. Rosenberg, D. Turnbull, T. J. B. Collins, P. B. Radha, P. W. McKenty, J. D. Zuegel, F. J. Marshall, S. P. Regan *et al.*, Wavelength-detuning cross-beam energy transfer mitigation scheme for direct drive: Modeling and evidence from national ignition facility implosions, *Phys. Plasmas* **25**, 056314 (2018).
- [32] W. Seka, H. A. Baldis, J. Fuchs, S. P. Regan, D. D. Meyerhofer, C. Stoeckl, B. Yaakobi, R. S. Craxton, and R. W. Short, Multibeam stimulated Brillouin scattering from hot, solid-target plasmas, *Phys. Rev. Lett.* **89**, 175002 (2002).
- [33] W. Seka, D. H. Edgell, J. F. Myatt, A. V. Maximov, R. W. Short, V. N. Goncharov, and H. A. Baldis, Two-plasmon-decay instability in direct-drive inertial confinement fusion experiments, *Phys. Plasmas* **16**, 052701 (2009).
- [34] W. Seka, J. F. Myatt, R. W. Short, D. H. Froula, J. Katz, V. N. Goncharov, and I. V. Igumenshchev, Nonuniformly driven two-plasmon-decay instability in direct-drive implosions, *Phys. Rev. Lett.* **112**, 145001 (2014).
- [35] M. N. Rosenbluth, Parametric instabilities in inhomogeneous media, *Phys. Rev. Lett.* **29**, 565 (1972).
- [36] S. Depierreux, C. Neuville, C. Baccou, V. Tassin, M. Casanova, P.-E. Masson-Laborde, N. Borisenko, A. Orekhov, A. Colaitis, A. Debayle *et al.*, Experimental investigation of the collective Raman scattering of multiple laser beams in inhomogeneous plasmas, *Phys. Rev. Lett.* **117**, 235002 (2016).
- [37] J. Zhong, H. Shiraga, and H. Azechi, One-dimensional and multichannels multi-imaging x-ray streak camera for imploded core plasma of shell-cone target, *Rev. Sci. Instrum.* **79**, 10E907 (2008).
- [38] R. Fabbro, C. Max, and E. Fabre, Planar laser-driven ablation: Effect of inhibited electron thermal conduction, *Phys. Fluids* **28**, 1463 (1985).
- [39] W. M. Manheimer, D. G. Colombant, and J. H. Gardner, Steady-state planar ablative flow, *Phys. Fluids* **25**, 1644 (1982).
- [40] P. Mora, Theoretical model of absorption of laser light by a plasma, *Phys. Fluids* **25**, 1051 (1982).
- [41] K. Fang, Z. Zhang, Y.-T. Li, and J. Zhang, Analytical studies of Rayleigh-Taylor instability growth of double-cone ignition scheme in 2020 winter experimental campaign, *Acta Phys. Sin.* **71**, 035204 (2022).
- [42] C. Zhang, Y. Zhang, X. Yuan, Z. Zhang, M. Xu, Y. Dai, Y. Dong, H. Gu, Z. Liu, X. Zhao *et al.*, Development of a monochromatic crystal backlight imager for the recent double-cone ignition experiments, *Chin. Phys. B* **33**, 025201 (2024).
- [43] See <http://www.prism-cs.com/for> information of the spectral analysis code PrismSPECT.

- [44] Z. Liu, F. Wu, Y. Zhang, X. Yuan, Z. Zhang, X. Xu, Y. Xue, J. Tian, J. Zhong, and J. Zhang, Observation of colliding process of plasma jets in the double-cone ignition scheme using an x-ray streak camera (unpublished).
- [45] R. Betti, V. Gopalaswamy, A. Lees, D. Patel, and J. Knauer, Exploring pathways to hydro-equivalent ignition on the omega laser, in *APS Division of Plasma Physics Meeting Abstracts*, APS Meeting Abstracts, Vol. 2020 (APS, New York, 2020), p. BO09.009.
- [46] H. Abu-Shawareb, R. Acree, P. Adams, J. Adams, B. Addis, R. Aden, P. Adrian, B. B. Afeyan, M. Aggleton, L. Aghaian *et al.*, Lawson criterion for ignition exceeded in an inertial fusion experiment, *Phys. Rev. Lett.* **129**, 075001 (2022).
- [47] W. Theobald, A. A. Solodov, C. Stoeckl, K. S. Anderson, F. N. Beg, R. Epstein, G. Fiksel, E. M. Giraldez, V. Yu. Glebov, H. Habara *et al.*, Time-resolved compression of a capsule with a cone to high density for fast-ignition laser fusion, *Nat. Commun.* **5**, 5785 (2014).